Construction of a stochastic model of track geometry irregularities and validation through experimental measurements of dynamic loading

Alfonso M Panunzio, Guillaume Puel, Régis Cottereau, Samuel Simon, Xavier Quost

To appear in *Vehicle System Dynamics*
Vol. 00, No. 00, Month 20XX, 1–26

Construction of a stochastic model of track geometry irregularities and validation through experimental measurements of dynamic loading

Alfonso M. Panunzio[a,b] , G. Puel[a], R. Cottereau[a] *, S. Simon[b] and X. Quost[b]

[a] *Laboratoire MSSMat, UMR CNRS 8579, CentraleSupélec, Université Paris-Saclay*
[b] *Régie autonome des transports parisiens (RATP)*

(*released month year*)

This paper describes the construction of a stochastic model of urban railway track geometry irregularities, based on experimental data. The considered irregularities are track gauge, superelevation, horizontal and vertical curvatures. They are modelled as random fields whose statistical properties are extracted from a large set of on-track measurements of the geometry of an urban railway network. About 300 to 1000 terms are used in the Karhunen-Loève/Polynomial Chaos expansions to represent the random fields with appropriate accuracy. The construction of the random fields is then validated by comparing on-track measurements of the contact forces and numerical dynamics simulations for different operational conditions (train velocity and car load) and horizontal layouts (alignment, curve). The dynamics simulations are performed both with and without randomly generated geometrical irregularities for the track. The power spectrum densities obtained from the dynamics simulations with the model of geometrical irregularities compare extremely well with those obtained from the experimental contact forces. Without irregularities, the spectrum is 10 to 50 dB too low.

Keywords: track geometry irregularities; railway vehicle dynamics; statistical validation

1. Introduction

The layout of a railway network is decided in the design phase according to engineering considerations. However the track evolves during its operational life because of train loads, weather conditions, substructure variations and maintenance interventions. In particular, track geometry irregularities appear and impact the dynamical response of a train [1–5], the rolling contact fatigue [6–8] and the rail corrugation [9]. In fact, even a small variation of the geometry can produce large changes of the rail-wheel contact patch and forces [10]. The maintenance policy of a railway line is very sensitive to track irregularities, especially on an urban line that is characterized by intense traffic and strongly variable operational conditions (velocity and passenger loads). Therefore, the track geometry is constantly monitored using different measurement systems [11–14].

Using information from measurements, it is possible to estimate the statistical properties of the track geometry and generate the irregularities as random fields indexed on space. The first step consists in extracting realizations of the fields from the measurements set and estimate the probability density functions and the spatial dependency

*Corresponding author. Email: regis.cottereau@centralesupelec.fr

(usually represented by the power spectral densities, PSDs). In many railway applications the irregularities are generated from the PSD as Gaussian fields [8, 15–18] using a spectral representation [19]. In [20] the geometry irregularities of a high-speed railway network have been generated as a non-Gaussian irregularities random field with a more complete dependence structure. The method proposed in [20] combines the Karhunen-Loève Expansion [21], to capture the spatial dependency, and the Polynomial Chaos Expansion [22] to obtain a good statistical representation of the non-Gaussian fields. This technique is used in this work to generate track geometries which are statistically representative of the RATP urban railway network (RER line A), operating in the Paris metropolitan area. The main differences between a high-speed and an urban railway network are the operational conditions (velocity, passengers loads and train passages frequency) and horizontal layout (curve frequency and radius). This implies a difference in the interactions between vehicles and track and the maintenance policies, and so the geometric irregularities. The main objective of this paper is to construct a stochastic model of the track geometry irregularities using experimental measurements.

In a second step the stochastic model is validated employing on-track wheel-rail forces measurements. The measurements of the geometry irregularities can be directly used as input for deterministic numerical computations to simulate the passage of the train on a real track portion [23–25]. Dynamic simulations, using the constructed random irregularities generator, are performed for different operational conditions using the multibody simulation software *SIMPACK*. A statistic characterisation of the wheel-rail contact forces is therefore obtained. For the validation of the irregularities model, the results of dynamic simulations are statistically compared with measurements of dynamic quantities of interest. These measurements are performed on a vehicle equipped with strain gauge systems positioned in the wheels [2, 26]. A comparison of the power spectral densities of the measured and the simulated contact forces is made to validate the stochastic model of the track irregularities.

The paper is organized into two parts: the Section 2 is dedicated to the track geometry measurement and random modelling, while in Section 3, in order to validate the model, the spectra of the simulated and experimental dynamic wheel-rail forces are compared.

2. Stochastic model of the track irregularities

The measurements used to extract the statistical features are firstly described in this section. Then, the statistics of the track irregularities and the technique used to construct a stochastic model of them are presented.

2.1. *Track geometry measurement data description*

By considering the rails as lines evolving in the space, the track geometry is the set of fields defining their position. Different choices can be made on these fields, but it is common, in the railway domain, to work with:

- Track gauge, $G(s)$, the spacing of the rails measured between the inner faces
- Superelevation, $E(s)$, the difference in height between the two rails
- Horizontal curvature, $C_H(s)$, referred to the track median line
- Vertical curvature, $C_V(s)$, referred to the track median line

where the indexation variable s is the curvilinear abscissa of track median line. A geometry irregularity is the difference between the design and the current geometry. In

some cases, instead of working with the curvatures irregularities, one can introduce two quantities: alignment ($al(s)$) and vertical profile ($lp(s)$). These quantities are defined as the double integral in space of the curvatures irregularities ($C_{Hirr}(s)$ and $C_{Virr}(s)$) and represent the displacement of the mean track line from its design position:

$$al(s) = \int\int C_{Hirr}(s)ds \quad ; \quad lp(s) = \int\int C_{Virr}(s)ds \tag{1}$$

The geometry irregularities are sketched in Figure 1.

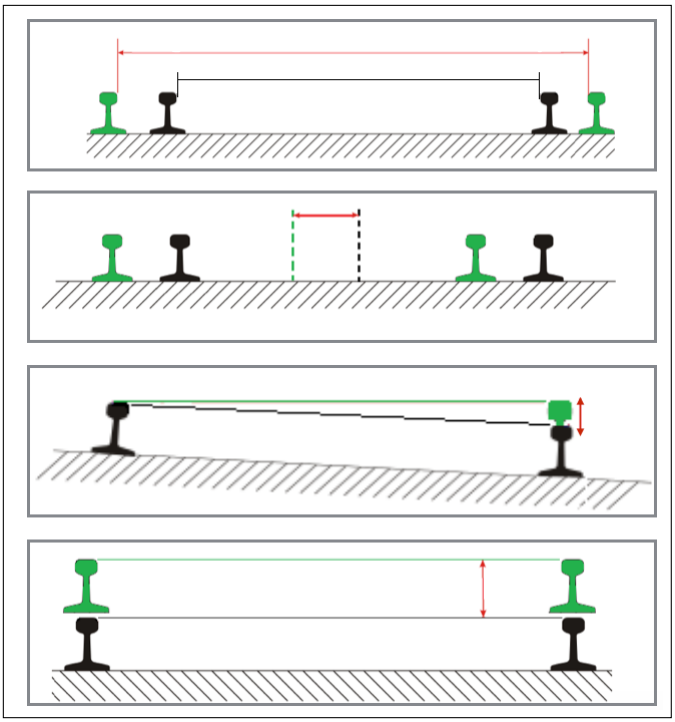

Figure 1. Sketch of track geometry irregularities (design position in black, irregular position in green). From top to bottom: gauge, alignment, superelevation, vertical profile.

2.1.1. Measurement system

The measurement train V355 system consists in a mobile rigid base equipped by two fibre optic gyroscopes and six laser cameras pointing the rails (three on each side). It is represented in Appendix A. The superelevation and the gauge are directly measured whereas the horizontal and vertical curvatures are obtained using a chord-based system [11]. This means that the curvatures are not directly measured, but they are linked to a versine measurement, $v(s)$, with a relation depending on the spatial frequency, f, that can be modelled with a transfer function, $H(f)$, and its associated impulsive response, $h(s)$ [27, 28]:

$$\begin{aligned} H(f) &= \frac{1}{(2\pi f)^2}\left(1 - \frac{A_2}{A_1+A_2}\exp(-2A_1\pi f\mathrm{i}) - \frac{A_1}{A_1+A_2}\exp(2A_2\pi f\mathrm{i})\right) \\ v(s) &= (h * C_H)(s) \qquad h(s) = \mathcal{F}^{-1}(H(f)) \end{aligned} \tag{2}$$

where A_1 and A_2 are the distances between the laser cameras (4.5 m and 5.5 m) and the symbol $*$ denotes the convolution product. The phase of this transfer function, shown in Figure 2, depends on the circulation direction because of the asymmetry of the system ($A_1 \neq A_2$). To avoid a noise amplification, the transfer function in Equation 2 is not brutally inverted but a Wiener deconvolution approach is employed [27, 29].

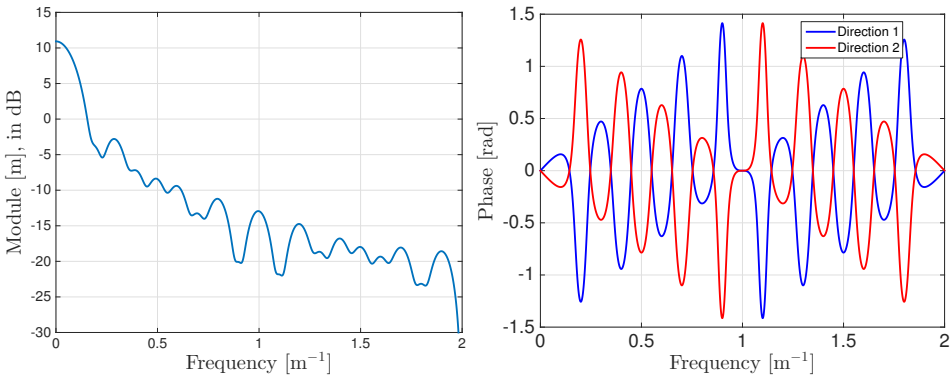

Figure 2. Curvature to versine transfer function (Equation 2): (left) module and (right) phase.

2.1.2. Measurement campaigns

All the measurement campaigns from 2005 to 2015 concerning the RER A railway network have been processed. This is an urban railway network crossing the Paris metropolitan area West to East (75 km double-track). Only the ballasted portions (93 % of the total length) are processed in this paper. The maximal operational velocity goes from 80 to 120 km/h according to the portion. With around 350 million of passengers per year, it is one of the busiest network in the world. During the considered period, the measurement train passed about 22 times on each point of the network. The passages of the train on the secondary (storage and intermediate) tracks and points and crossings have been suppressed. At the end about 9 millions of measurement points, recorded with a sampling rate equal to 0.25 m, are considered for the statistical model. An example of the track geometry measures with the corresponding theoretical (design) values is shown in Figure 3.

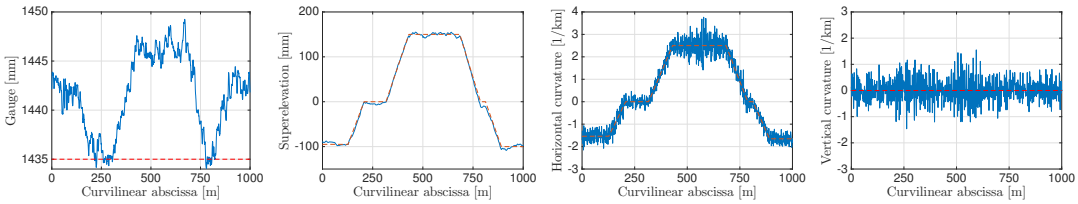

Figure 3. Example of track geometry measurement with corresponding theoretical values (dashed red line), from left to right: gauge, superelevation, horizontal curvature and vertical curvature.

2.2. *Statistical description of the track geometry measurements*

After collecting the measurements data, realizations of the geometry fields can be extracted from the measurement campaigns. The irregularities of superelevation, horizontal

and vertical curvatures are defined as the differences between the measurements and the corresponding design (or theoretical) known values:

$$\begin{cases} E(s) = E_d(s) + E_{irr}(s) \\ C_H(s) = C_{Hd}(s) + C_{Hirr}(s) \\ C_V(s) = C_{Vd}(s) + C_{Virr}(s) \end{cases} \tag{3}$$

where the subscripts $_d$ and $_{irr}$ indicate respectively the design values and the irregularities fields.

Concerning the gauge, the design value is equal to 1435 mm on the whole line. However the measurements show that the gauge tends to increase in the curved track portions. In fact, the correlation coefficient between the gauge measurements and the horizontal design curvature $|C_{Hd}(s)|$ (taken in absolute value to equally consider leftward and rightward curves) is equal to 0.57 (while for the other irregularities it is lower than 0.02). The correlation table of the irregularities fields and the design curvature is shown in Figure 4. Therefore the gauge field is separated into two terms. One of them, $G_0(|C_{Hd}(s)|)$, depends on the design curvature and is calculated by linear regression, while the other one, $G_{irr}(s)$, is the irregularity field that is decorrelated from the curvature and has to be modelled:

$$\begin{cases} G(s) = G_d + G_0(|C_{Hd}(s)|) + G_{irr}(s) \\ G_0(|C_{Hd}(s)|) = 3.97|C_{Hd}(s)| \text{ mm}\cdot\text{km} \end{cases} \tag{4}$$

with the curvature expressed in km^{-1}.

$\lvert C_{Hd}\rvert$	0.57	0.04	0.01	0.00	0.01
	G	0.44	0.03	0.01	0.05
		G_{irr}	0.01	0.00	0.02
			E_{irr}	0.03	0.00
				C_{Hirr}	0.01
					C_{Virr}

Figure 4. Correlations (at spatial lag equal to zero) between the design horizontal curvature ($|C_{Hd}(s)|$), the gauge measure (G) and the irregularities fields (gauge G_{irr}, superelevation E_{irr}, horizontal curvature C_{Hirr} and vertical curvature C_{Virr}).

The irregularities fields thus defined are centred and decorrelated from the horizontal layout of the track. Their experimental histogram, here used as probability densities functions (PDFs), are shown in Figure 5. The marginal PDFs of the fields are not Gaussian.

The cross-correlations between the irregularities are small (lower than 0.05 at zero lag, Figure 4). The experimental joint PDFs (at zero lag), Figure 6, show that there are not strong dependencies between the fields. Therefore, the dependences between the irregularities are neglected in this work and the fields are identified separately.

The experimental correlation functions, Figure 7, show that the correlation length of each field is different: around 200 m for the superelevation and the gauge, less than 20 m

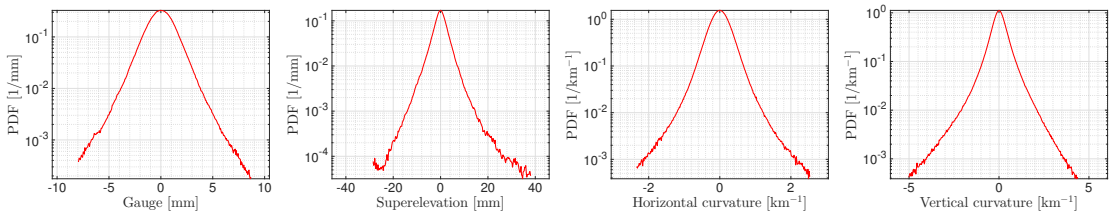

Figure 5. Experimental PDFs of geometry irregularities, from left: gauge, superelevation, horizontal curvature and vertical curvature.

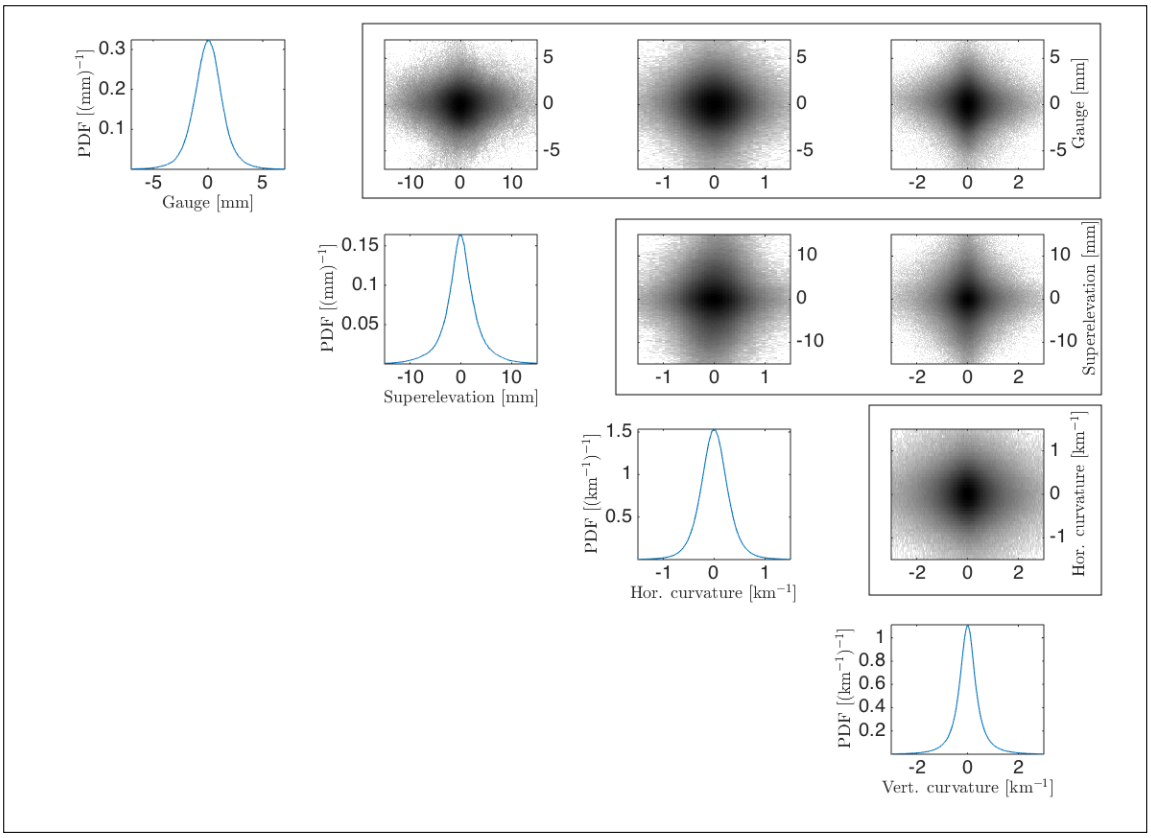

Figure 6. Joint PDFs of the track irregularities (at zero lag). Logarithmic color scale.

for both the curvatures. The corresponding experimental power spectral densities (PSDs) are shown in Figure 8.

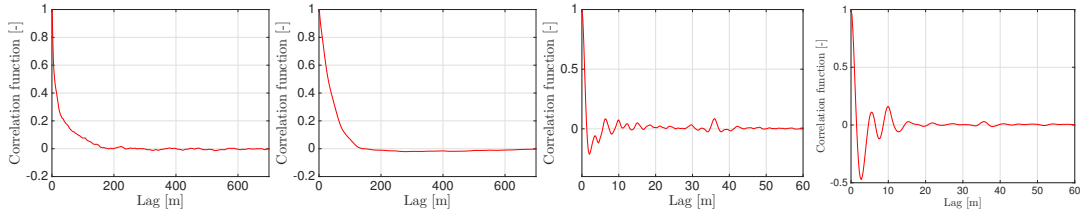

Figure 7. Correlation function of geometry irregularities, from left: gauge, superelevation, horizontal curvature and vertical curvature. Different scales of the lag axis (x).

The superelevation and the gauge correlation functions, which have a decreasing exponential behaviour, show that these irregularities are more related to the topography of the track. Similar irregularities PSDs can be found in [8, 17, 30]. Note however that the

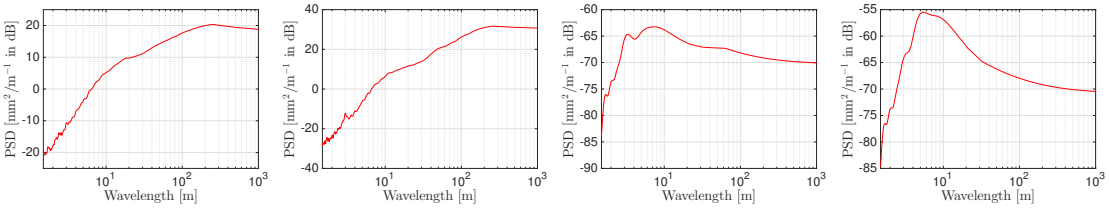

Figure 8. Experimental PSD of geometry irregularities, from left: gauge, superelevation, horizontal curvature and vertical curvature.

correlation length of the horizontal design track curvature is more than three time larger (Figure 9) and shows that there are not components of the irregularities correlated with the horizontal layout.

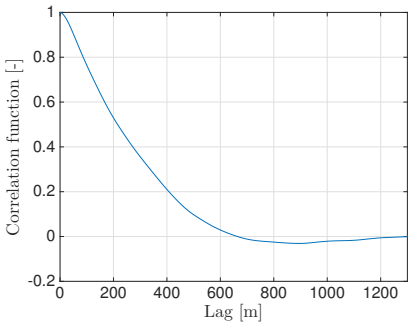

Figure 9. Correlation function of design horizontal curvature.

The curvatures irregularities are more related to the rail short lengths such as corrugation and welds [16, 31, 32]. The histogram of the length between two welds (on the considered railway network) superposed with the correlation of the horizontal curvature is shown in Figure 10. Note the correspondence between the histogram and the correlation function peaks. In the literature, the alignment *al* and the vertical profile *lp* (Equation 1) are often used instead of the horizontal and vertical curvatures. The PSDs of these quantities, obtained from the curvatures measurements, are shown in Figure 11 with the two German PSDs analytical standard that are usually used for simulation in European countries [33, 34]. A strong correspondece between them can be observed especially in the length range from 3 m to 40 m.

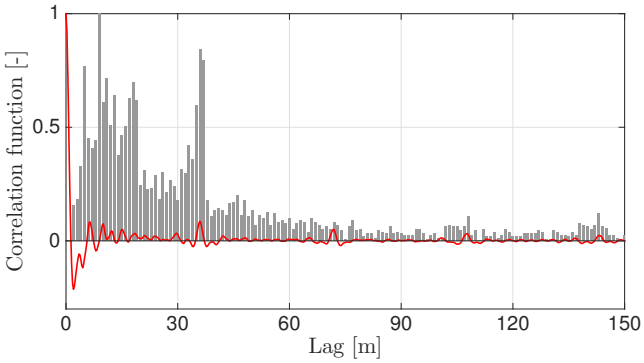

Figure 10. Histogram (normalized) of the length between two welds superposed with the correlation of the horizontal curvature irregularity.

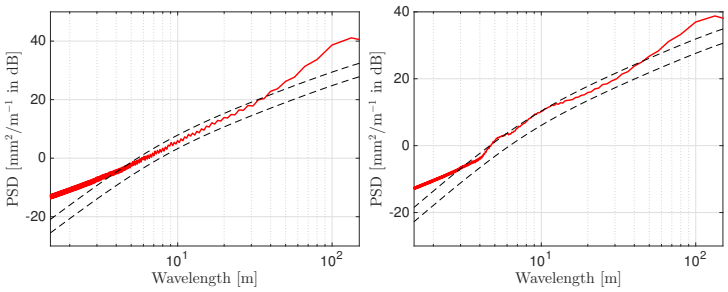

Figure 11. PSDs of alignment (left) and vertical profile (right). The dashed black lines represents two German PSDs standard [33, 34].

The weather influence on the track geometry has been analysed by estimating their statistics taking the measurements in the summer and winter seasons separately. No differences have been observed. That is why the weather is not considered into the model. Around 35 % of the line is in tunnels where no significant temperature variations are registered. The rest of the line is essentially composed by continuous welded rails, in which only the breathing zones can be thermally deformed along the longitudinal direction. This deformation does not influence the track geometry (rails positions in the lateral and vertical directions).

2.3. *Parametric model of the random fields*

In this paper the fields generator is constructed by combining the Karhunen-Loève expansion (KLE) and the Polynomial Chaos Expansion (PCE). This strategy has been successfully applied to model the track irregularities of a high speed railway network [20].

2.3.1. Karhunen-Loève expansion

Using a Karhunen-Loève expansion [21], a random field $f(s)$ (that could be any irregularity field) is approximated by its truncated projection on an orthogonal basis. In this way it is expressed as a sum of M deterministic spatial (depending only on the curvilinear abscissa) functions $\varphi_i(s)$ multiplied by random decorrelated and normalized coefficients η_i:

$$\begin{aligned} f(s) &\approx \sum_{i=1}^{M} \sqrt{\lambda_i}\varphi_i(s)\eta_i \\ \int_0^L C(s,s')\varphi_i(s')ds' &= \lambda_i\varphi_i(s) \qquad \mathbb{E}[\eta_i\eta_k] = \delta_{ik} \end{aligned} \tag{5}$$

where $s, s' \in [0, L]$, $C(s, s')$ is the covariance function associated with the field, δ_{ik} is the Kronecker delta and $\mathbb{E}$ denotes the expectation operation. In a more compact form, this expansion is written as:

$$f(s) \approx \boldsymbol{\Phi}(s)\sqrt{\boldsymbol{\Lambda}}\boldsymbol{H} \tag{6}$$

where $\boldsymbol{\Phi}(s)$ is a M-dimensional row vector such that $\Phi_l(s) = \varphi_l(s)$, $\boldsymbol{\Lambda}$ is a $M \times M$ diagonal matrix such that $\Lambda_{lm} = \delta_{lm}\lambda_l$ and $\boldsymbol{H}$ is a M-dimensional column vector such that $H_l = \eta_l$

This expansion reduces the normalized mean-square error ε_{KL} resulting of its truncation that, thanks to the orthogonality property of the basis, can be expressed as:

$$\varepsilon_{KL} = 1 - \frac{\sum_{i=1}^{M} \lambda_i}{\mathbb{E}[f(s)^2]} = \frac{\int (S(f) - S_g(f)) df}{\int S(f) df} \tag{7}$$

where $S(f)$ and $S_g(f)$ are respectively the reference (estimated from measurements) and the modelled PSDs. The error on the PSDs (chosen equal to 1%) only depends on the truncation error of the KLE.

The length L in Equation 5 is different for each irregularity field because of the different correlation lengths (Figure 7). It is set to three times the correlation length. Taking a larger length does not change the statistical properties but would require more terms in the KLE. The threshold for the truncation error is set to 1% in this work. This error is evaluated for the four fields separately (Figure 12). The field which needs more terms to be identified is the gauge (314 terms to obtain a truncation error equal to 0.01). The first (most energetic) three modes (deterministic functions $\varphi_i(s)$) associated with each field are shown in Figure 13. Note the different lengths of the modes according to the field.

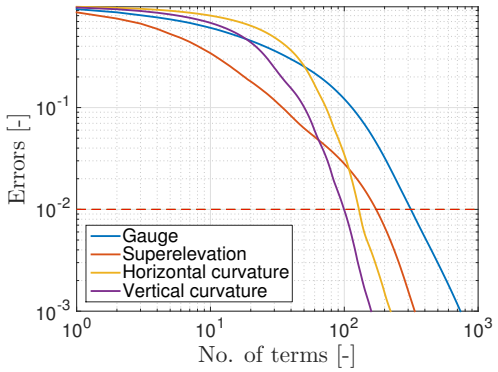

Figure 12. Karhunen-Loève truncation errors.

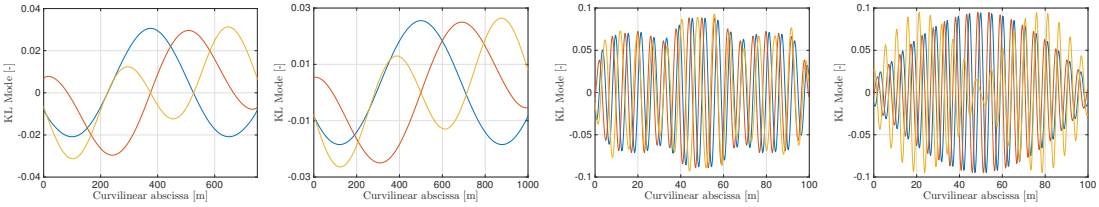

Figure 13. First (most energetical) three Karhunen-Loève modes (blue, red and yellow lines in the energetical order), from left: gauge, superelevation, horizontal curvature and vertical curvature.

2.3.2. Polynomial Chaos expansion

If a random field is Gaussian, then the coefficients η_i are independent standard Gaussian variables. In a general case their distribution has to be identified. The multivariate distributions of the random projection coefficients (η_i) of the basis of each random field are characterized using the PCE [22]. This consists in expanding the random coefficients in a sum of deterministic coefficients β_{ij} multiplied by a polynomial basis ψ_j of multivariate

germs $\boldsymbol{\xi}$ (whose probability density function is chosen a priori):

$$\eta_i \approx \sum_{j=1}^{N} \beta_{ij} \psi_j(\boldsymbol{\xi}) \tag{8}$$

The polynomial functions are chosen such that they are orthogonal with respect to the distributions of the germs. For instance, Hermite polynomials are chosen with normal germs while Legendre polynomials are chosen with uniform germs. Given the number of germs n_g and the polynomial degree d the number of polynomials N is:

$$N = \frac{(n_g + d)!}{n_g! d!} \tag{9}$$

In a more compact form, the Equation 8 is written as:

$$\boldsymbol{H} = \mathbf{B}\,\boldsymbol{\Psi}(\boldsymbol{\xi}) \tag{10}$$

where $\boldsymbol{\Psi}(\boldsymbol{\xi})$ is a N-dimensional column vector such that $\Psi_l(\boldsymbol{\xi}) = \psi_l(\boldsymbol{\xi})$ and $\mathbf{B}$ is a $M \times N$ matrix such that $B_{lm} = \beta_{lm}$.

Since the number of coefficients (dimension of the random space to characterize) is very high, advanced techniques to identify the deterministic coefficients are employed to guarantee a good representation [35, 36]. These coefficients are thus chosen as the argument that maximizes the log-likelihood between the available realisations of the random coefficients and their chaos representation. Because of the decorrelation and the normalization properties due to the KLE (Equation 5) the following constraint has to be satisfied:

$$\mathbf{B}\mathbf{B}^{\mathrm{T}} = \mathbf{I} \tag{11}$$

where $\mathbf{I}$ is the identity matrix.

For each KLE coefficient the Kullback-Leibler distance [37], evaluated in the range of the 0.1th l and the 99.9th u percentiles of the target PDF, can be used to define an error ϵ_i between the target (obtained from measurements) and the generated PDFs. The maximal value of this error, on all the KLE coefficients, is taken as PCE identification error ε_{PCE}:

$$\begin{aligned} \epsilon_i &= \int_l^u p(x) \ln\left(\frac{p(x)}{q(x)}\right) dx \\ \varepsilon_{PCE} &= \max(\epsilon_i) \end{aligned} \tag{12}$$

where $p(x)$ and $q(x)$ are the target and the generated PDFs. Choosing a threshold tolerance τ (0.01 in this work), the number of germs and the polynomial degree are chosen as:

$$(n_g, d) = \arg\min(N(n_g, d) \,|\, \varepsilon_{PCE} < \tau) \tag{13}$$

For instance, in Figure 14, the value of the error ε_{PCE} defined in Equation 12 is shown for different numbers of germs and polynomial degrees in the case of the vertical curvature. Note that, when the number of PCE terms is lower than the number of KLE

Table 1. Number of terms used in the random fields model. KLE truncation error $\varepsilon_{KL} = 0.01$

No. of terms	KLE	PCE (Hermite)	PCE (Legendre)
Gauge	314	1001 (4 germs, degree 10)	1287 (5 germs, degree 8)
Superelevation	173	495 (4 germs, degree 8)	1001 (4 germs, degree 10)
Horizontal curvature	129	495 (4 germs, degree 8)	715 (4 germs, degree 9)
Vertical Curvature	100	330 (4 germs, degree 7)	495 (4 germs, degree 8)

terms to model ($N < M$), the identification is not possible since the Equation 11 cannot be satisfied.

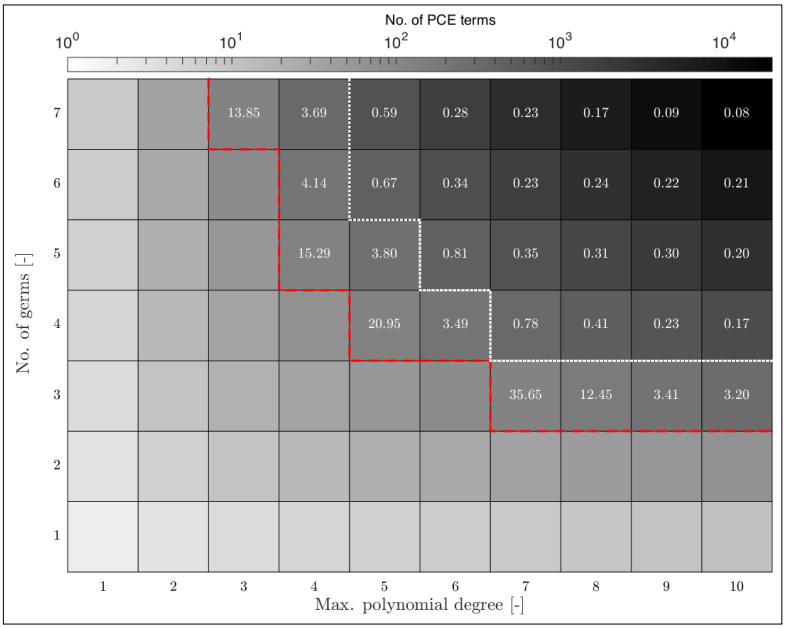

Figure 14. Percentage error in the PCE identification (ε_{PCE} in Equation 12) of the vertical curvature irregularity (100 KLE terms). The dashed red line delimits the area in which the identification is not possible since the number of PCE terms is lower than the number of KLE terms to model. The dotted white line delimits the area in which the PCE error is lower than 1%.

The number of KLE and PCE terms (with Hermite and Legendre polynomial basis) for each field are shown in Table 1. Using Legendre polynomials (and so uniform germs) requires more terms to obtain the same accuracy. Therefore, Hermite polynomials (and so Gaussian germs) are chosen for the model.

2.4. *Random generation*

The germs distribution determines the polynomial family used as basis. In this work Gaussian germs and so Hermite polynomials are employed. Finally, by generating ν germs $\boldsymbol{\xi}$ it is possible to obtain ν independent realisations of the generated field $f_{gen}(s)$:

$$f_{gen}(s) = f_d(s) + f_0(|C_{Hd}(s)|) + \sum_{i=1}^{M}\sum_{j=1}^{N}\sqrt{\lambda_i}\varphi_i(s)\beta_{ij}\psi_j(\boldsymbol{\xi}) \tag{14}$$

where $f_d(s)$ and $f_0(|C_{Hd}(s)|)$ are respectively the design value and the component, not null for the gauge, correlated to the design horizontal curvature.

2.4.1. Generation with an arbitrary length

The length of the generated fields, L, is set by the integration interval on which the Karhunen-Loève expansion is defined (Equation 5). However, one usually needs to generate a field longer (L_{new}) than that length. The simple concatenation of more realisations will break the continuity of the field and the correlation structure around the breaking points. The generation method described in [38], originally proposed to generate cross-correlated random fields, is here adapted to be used to outcome this issue in the case of stationary random fields. The main steps of the adapted method are here summarized:

- Define the function:

$$\tilde{C}(|s-t|) = \begin{cases} C(|s-t|), & \text{if } |s-t| \leq L \\ 0, & \text{if } |s-t| > L \end{cases} \tag{15}$$

  where $C(|s-t|)$ is the covariance function of the considered field.
- Define the $M \times M$ matrix $\mathbf{K}$ such that:

$$\begin{aligned} K_{lm} &= \frac{1}{\sqrt{\lambda_l \lambda_m}} \int_0^L \int_L^{2L} \tilde{C}(|s-t|)\varphi_l(s)\varphi_m(t-L)dsdt \\ &= \frac{1}{\sqrt{\lambda_l \lambda_m}} \int_0^L \int_0^L \tilde{C}(|s-t-L|)\varphi_l(s)\varphi_m(t)dsdt \end{aligned} \tag{16}$$

- Generate, as in Equation 10, a n-dimensional set (such that $nL > L_{new}$) of KLE coefficients: $\boldsymbol{H}^{(k)} = \mathbf{B}\,\boldsymbol{\Psi}(\boldsymbol{\xi}^{(k)})$, with k going from 1 to n.
- Define the $2nM \times 2nM$ matrix $\mathbf{R}$ such that:

$$\mathbf{R}\mathbf{R}^{\mathrm{T}} = \begin{bmatrix} \mathbf{I} & \mathbf{K} & & \cdots & \mathbf{0} \\ \mathbf{K}^{\mathrm{T}} & \mathbf{I} & \mathbf{K} & & \vdots \\ & \ddots & \ddots & \ddots & \\ \vdots & & \mathbf{K}^{\mathrm{T}} & \mathbf{I} & \mathbf{K} \\ \mathbf{0} & \cdots & & \mathbf{K}^{\mathrm{T}} & \mathbf{I} \end{bmatrix} \tag{17}$$

  where $\mathbf{0}$ is a $M \times M$ null matrix.
- Define a n-dimensional set of transformed KLE coefficients $\tilde{\boldsymbol{H}}$ such that:

$$\begin{bmatrix} \tilde{\boldsymbol{H}}^{(1)} \\ \vdots \\ \tilde{\boldsymbol{H}}^{(k)} \\ \vdots \\ \tilde{\boldsymbol{H}}^{(n)} \end{bmatrix} = \mathbf{R} \begin{bmatrix} \boldsymbol{H}^{(1)} \\ \vdots \\ \boldsymbol{H}^{(k)} \\ \vdots \\ \boldsymbol{H}^{(n)} \end{bmatrix} \tag{18}$$

- Finally, the field $g(s)$ (of length L_{new}) is generated as:

$$g(s) = \begin{cases} \boldsymbol{\Phi}(s)\sqrt{\boldsymbol{\Lambda}}\tilde{\boldsymbol{H}}^{(1)}, & \text{if } 0 \leq s \leq L \\ \vdots & \vdots \\ \boldsymbol{\Phi}(s-(k-1)L)\sqrt{\boldsymbol{\Lambda}}\tilde{\boldsymbol{H}}^{(k)}, & \text{if } (k-1)L < s \leq kL \\ \vdots & \vdots \\ \boldsymbol{\Phi}(s-(n-1)L)\sqrt{\boldsymbol{\Lambda}}\tilde{\boldsymbol{H}}^{(n)}, & \text{if } (n-1)L < s \leq L_{new} \end{cases} \tag{19}$$

This method works under the condition that, for a spatial lag larger than L, the correlation function of the field can be approximated to zero. The covariance function of the field $g(s)$ is equal to $\tilde{C}(|s-t|)$ (defined in Equation 15) on all the domain. This is due to the fact that, by construction:

$$\begin{aligned} &\mathbb{E}[\tilde{\boldsymbol{H}}^{(k)}] = \boldsymbol{0} \\ &\mathbb{E}[\tilde{\boldsymbol{H}}^{(k)}(\tilde{\boldsymbol{H}}^{(l)})^{\mathrm{T}}] = \begin{cases} \mathbf{I}, & \text{if } k = l \\ \mathbf{K}, & \text{if } k = l-1 \\ \mathbf{K}^{\mathrm{T}}, & \text{if } k = l+1 \\ \mathbf{0}, & \text{otherwise} \end{cases} \end{aligned} \tag{20}$$

where $\boldsymbol{0}$ is a M-dimensional null column vector.

Even if the field $g(s)$ is defined as piecewise, its continuity is guaranteed also at the breaking points when $M \to \infty$. For a discussion about the continuity see Appendix B.

2.5. *Comparison with measurements*

The KLE allows to capture the spatial correlation of the fields and the PCE ensures the statistical variability of the track geometry: the obtained realisations are representative of a whole railway network. The PSDs and the marginal distribution of the four fields are shown in Figure 15 and Figure 16. The frequencies that are not properly represented have an energetic level about 20 dB lower than the maximal power. With a KLE truncation error chosen equal to 1%, the curvature fields are correctly represented in the spectrum range of interest (wavelengths between 1 m and 150 m), differently from the gauge and the superelevation. Although taking more terms would decrease the error, the effect of more terms on the dynamic forces spectra is limited (as shown in Section 3.3).

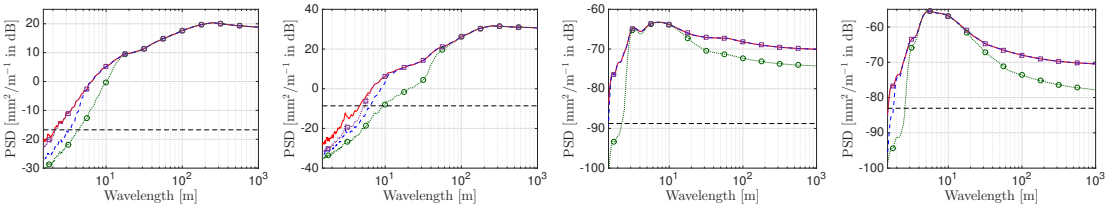

Figure 15. PSDs of geometry irregularities, from left: gauge, superelevation, horizontal curvature and vertical curvature. Measurements (red line), generations with 10% (dotted green line with circle markers), 1% (dashed blue line) and 0.1% (dotted violet line with square markers), 1% of the mean spectral density (horizontal dashed black line).

The error on the distributions, that is evaluated using the Kullback-Leibler distance, depends on the PCE identification and is indicated in Figure 16. It is shown that the

model is able the capture the distribution tails. Note that the condition used in Equation 13 concerns the maximal distance of all the KLE coefficients and not the distance on the marginal PDFs of the field. This means that all the modes, even the less energetic ones, are properly represented.

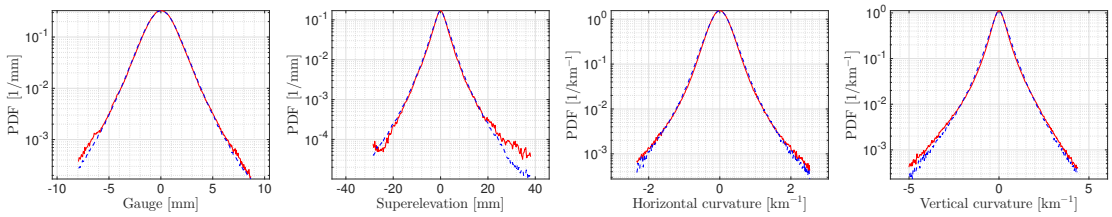

Figure 16. PDFs of geometry irregularities, from left: gauge, superelevation, horizontal curvature and vertical curvature. Measurements (red line), generations (dashed blue line).

Some examples of measured and generated irregularities are shown in Figure 17.

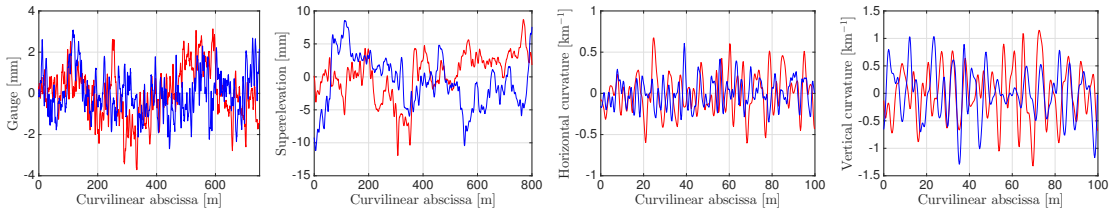

Figure 17. Example of geometry irregularities, from left: gauge, superelevation, horizontal curvature and vertical curvature. Measurements (red line), generations (blue line).

3. Dynamic simulations and validation

In this section, track irregularities stochastic model, described in Section 2, is validated through dynamical simulations. Measurements of the wheel-rail contact forces are collected on the same railway network on which the random generator is built. The goal is to compare the experimental spectra of the contact forces with the ones obtained by simulating the passage of the train on tracks modelled with random irregularities.

3.1. *Wheel-rail contact forces experimental data*

3.1.1. Measurement system

The wheel-rail contact forces are usually decomposed in the track frame into vertical (Q), lateral (Y) and longitudinal (X) directions (Figure 18). An adapted train running on the RER rail network (MI 2N unit) is used to measure the wheel-rail contact forces. The leading passenger car and the motor coach, which is positioned behind the passenger car, are instrumented. These vehicles have two bogies and four wheelsets as sketched in Figure 19. The wheels of the front bogies are drilled and equipped with strain gauges (Figure 3.1.1) able to measure the deformations which are processed to obtain the contact forces. The rear bogies are equipped with strain gauges located on the axle boxes. The measurement of the forces on the rear bogies is less precise than the front ones, because the gauges are more distant from the wheel-rail contact interface and they are filtered by

the wheelset (that is not infinitely rigid). In this work the validation will be performed by using the measures from the strain gauges located in the wheels (front bogies).

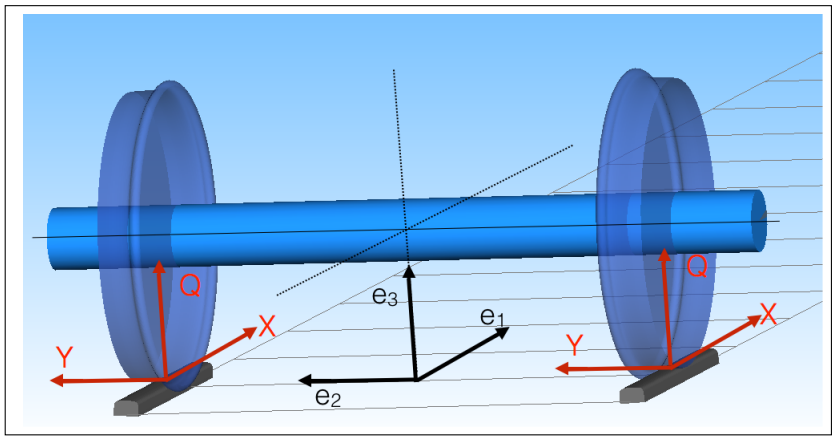

Figure 18. Contact forces decomposition (red) and track reference frame (black).

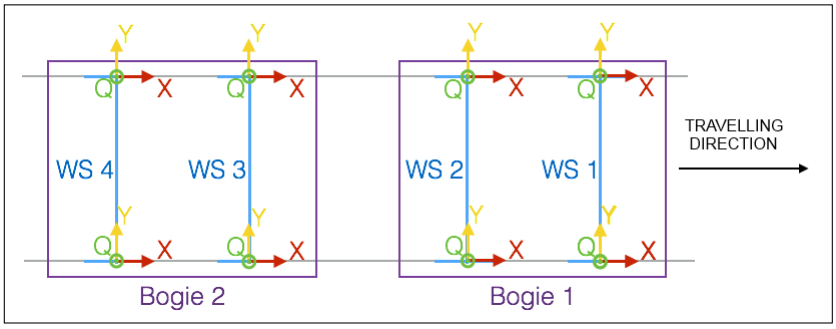

Figure 19. Measurement vehicle schema.

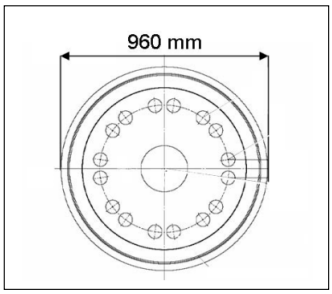

Figure 20. Position of the strain gauges used for the contact forces measurement on a wheel.

The angle between the two cars is measured and used to correctly locate the train on the track. In fact the angle signal is strongly correlated with the horizontal curvature of the track, i.e. the spatial lag between angle and horizontal curvature is given by the peak of their cross-correlation function. An example of the measured forces on a track portion with three curves is shown in Figure 21. As observed in this figure, the curve radius has a big impact on the forces fluctuations and their mean values (especially for the front wheelset which guides the bogie in the curve inscription) introducing a strong spatial non-stationarity. Examples of wheel-rail contact positions in a curved track are shown in Figure 22.

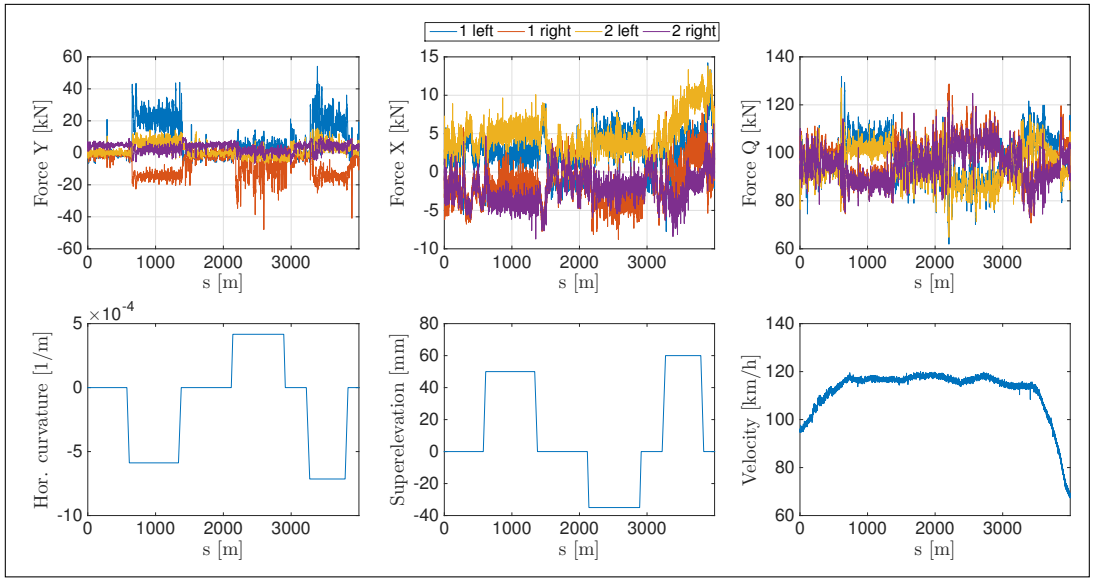

Figure 21. Example of the measured contact forces (front wheelset, front bogies, leading car) with the corresponding horizontal curvature, superelevation and train velocity.

3.1.2. Measurement campaigns

The measurements are performed on the RER line A (the same network on which the geometry is measured by the other recording train) at different operating conditions (maximal running velocity going from 80 to 120 km/h), in order to be representative of the trains circulating the this railway network.Two levels of weight of the leading car are used in the campaigns to simulate the passenger load: empty and charged (6 passengers per m^2, i.e. 20960 kg). The totality of the measurements corresponds to 1172 km of track travelled (630 km with an empty leading car and 542 with a charged one).

3.2. *Comparison of the power spectral densities of the contact forces*

The measurements of the dynamic forces are compared with numerical simulations where the track geometry are generated as in Section 2.4. To compute the dynamical forces, an advanced semi-Hertzian contact model [39] is used in the simulations. In this model the rail profile is discretized in strips along the lateral direction. Then, in each strip, the contact problem is solved as Hertzian. The railway dynamics software *SIMPACK* is used for this purpose.

The geometry irregularities are the only variable parameters in the simulations. In reality, other track parameters should be considered as stochastic to refine the simulations, but, since the objective is to validate the geometry irregularities model, these other parameters are used as deterministic. The rail profile (UIC60) is considered as theoretical, i.e. the wear is not included. The wheel-rail friction coefficient varies neither along the rail profile nor along the curvilinear abscissa of the track: it is equal to 0.2 in all the simulations. The rail cant is set to 1/20 (standard in France) and does not vary dynamically.

A multi-body model representative of the passenger car of the MI 2N train (circulating on the RER A railway network) is used for the simulations. The vehicle is composed by a car enclosure supported by two bogies equipped by two wheelsets each. The stiffness and the damping of the primary and secondary suspensions are set to the manufacturer data in all the simulations. The curb weight of this vehicle is approximatively equal to 55 t.

To take into account the weight of the measurement system, 4 t uniformly distributed in the car enclosure have been added.

At this stage the objective is to validate the geometry irregularities model by comparing numerical simulations to measurements. For this purpose all the measurement campaigns (Section 3.1.2) are replicated by simulating the passage of the vehicle on a track affected by geometry irregularities. Therefore, in each simulation the track design (nominal curvatures, gauge and superelevation), the weight and the running velocity are the same as in the corresponding measurement campaign, while the geometry irregularities are randomly generated according to the model presented in Section 2.4.

In this section we analyse the spectral densities of the contact forces in the length range from 1 m to 150 m (largest correlation length of the irregularities fields). The train dynamics strongly changes according to the curve radius (and the associated superelevation) and the velocity, as shown in Figure 21. For this reason, the PSDs are separately computed in straight and curved (outer and inner rails) track portions for constant velocities, acceleration and breaking phases.

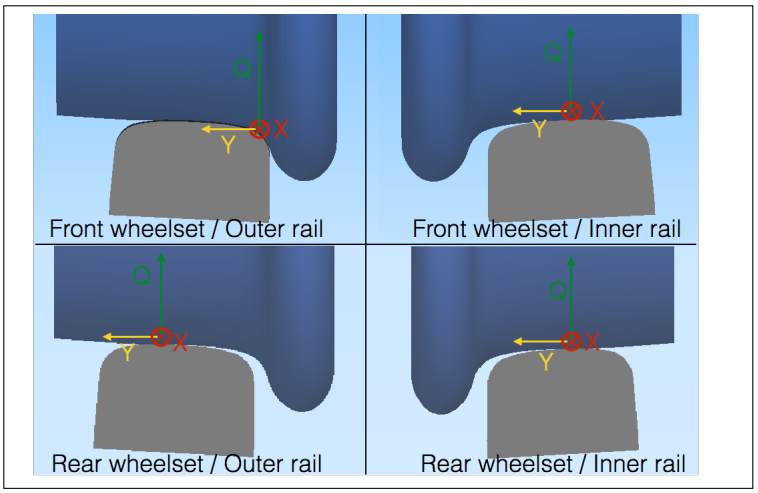

Figure 22. Example of contact positions in a curved track

3.2.1. Straight track

The PSDs of the contact forces on the front wheelset in straight track portions rolling at constant velocity are shown in Figure 23. When the geometry irregularities are taken into account in the simulations, a strong improvement is produced on the PSDs for the three components of the contact force. In the simulations performed without irregularities, the spectra of the contact forces are between 1 and 2 orders of magnitude smaller.

Some peaks appear, especially on the PSD of the longitudinal forces X, at a length corresponding to the wheel circumference and its submultiples. The wheel nominal diameter is equal to 0.42 m. These peaks seem to be due to wheel untrueness (see Section 3.4).

Another discrepancy, observable on the spectrum of the longitudinal force X between the lengths of 7 m and 50 m, could be due to the train traction system which is not considered in the simulations. As shown in [40], the motor traction effects affect the longitudinal equilibrium of the train in alignment by modifying the contact location and so the rolling radius.

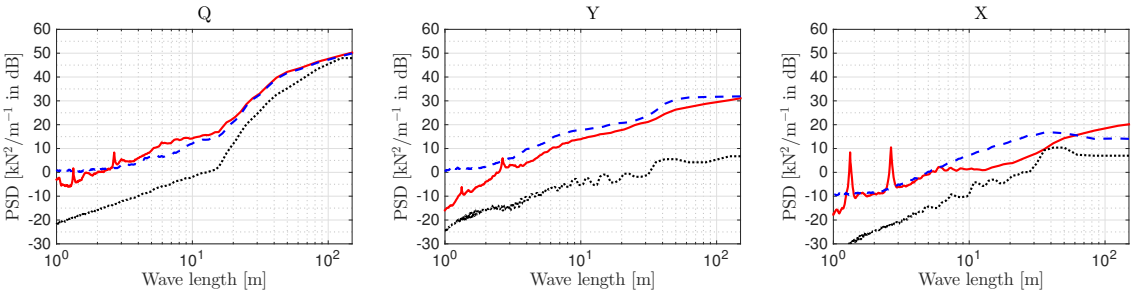

Figure 23. PSD of contact forces, front wheelset in alignment, constant velocity. Experimental data (red line), numerical simulations with (dashed blue line) and without (dotted black line) irregularities.

3.2.2. Curved track

The PSDs of the contact forces on the front wheelset in curved track portions rolling at constant velocity are shown in Figure 24. In a curved track the variability of the contact forces is larger than a straight track especially for the lateral Y forces on the outer rail. In fact, due to the localisation of the contact on the wheel flange, a small variation of the wheel-rail position causes larger changes of the contact force. When the irregularities are not considered the contact position is more stable. The random model of the irregularities allows to very well represent the forces spectra on all the wavelength range.

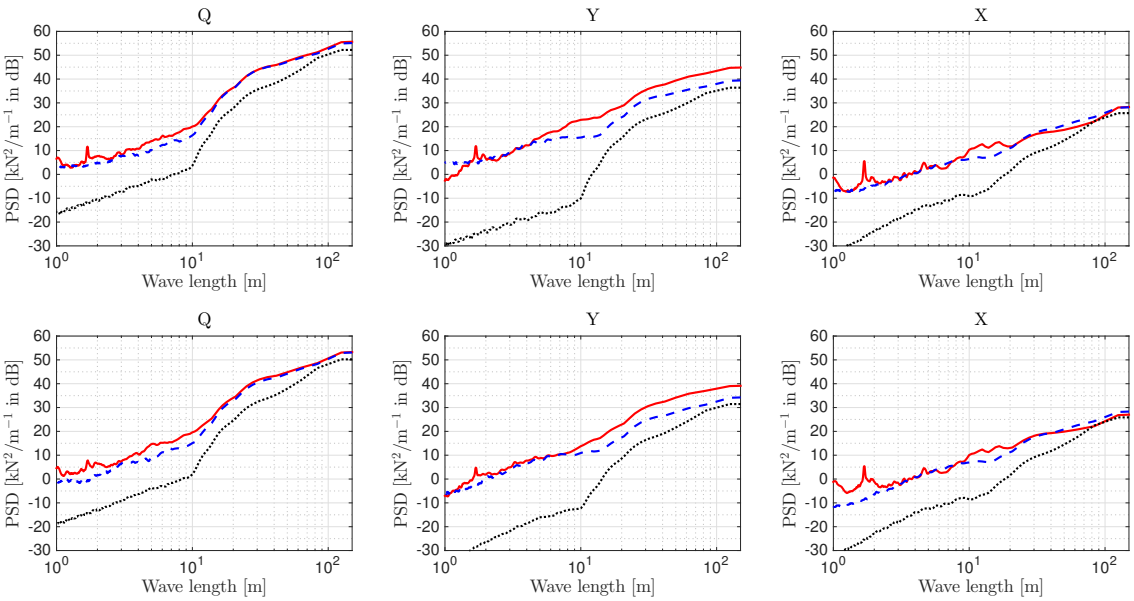

Figure 24. PSD of contact forces, front wheelset in curve (1st row outer rail, 2nd row inner rail), constant velocity. Experimental data (red line), numerical simulations with (dashed blue line) and without (dotted black line) irregularities.

3.2.3. Acceleration and braking

The PSDs of the contact forces on the front wheelset in straight track portions rolling in acceleration and breaking phases are shown in Figure 25. In the acceleration phases the difference between the experimental and the simulated PSDs is more important on the vertical and longitudinal forces, especially at the shorter wave lengths.

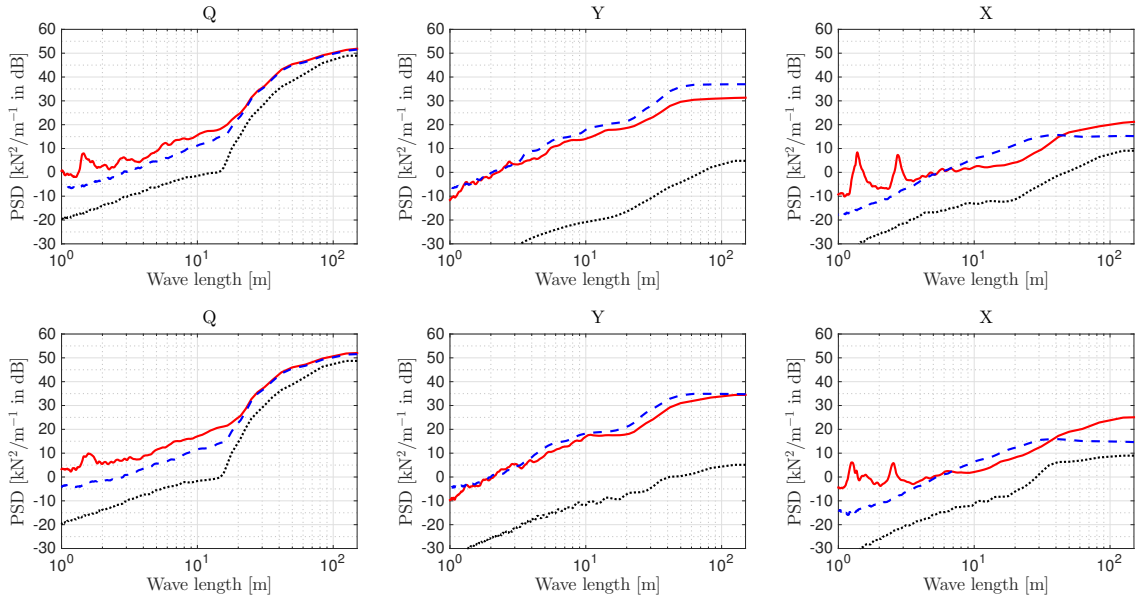

Figure 25. PSD of contact forces, front wheelset in alignment, variable velocity (1st row acceleration, 2nd row breaking). Experimental data (red line), numerical simulations with (dashed blue line) and without (dotted black line) irregularities.

3.3. *Influence of the number of Karhunen-Loève terms*

The numerical simulations with irregularities have been performed with different numbers of considered KLE terms and so different spectral energy relative errors: 10% and 0.1% instead of 1%. The number of needed terms is shown in Table 2 and the evolution of the truncation error according to number of terms is shown in Figure 12. When more terms are taken to divide by 10 the error, no significant changes are observed on the PSDs (Figure 26), but only a little improvement on the vertical force spectrum. In fact, as shown in [41], the vertical force is mostly sensitive to the superelevation and adding more terms reduces the spectral error on the wavelengths lower than 10 m. The other forces, Y and X are mostly sensitive to the horizontal curvature, which is already well represented on the considered spectral band with a KLE error equal to 1%. When more KLE terms are neglected the spectral energy is lower, especially for the lateral force Y. Indeed, the lateral forces are mostly sensitive to the horizontal curvature irregularities [41] whose PSD is badly represented for almost all the wavelengths when a KLE truncation equal to 10% is chosen (Figure 8).

Table 2. Number of terms used in the random fields model with two different KLE truncation error, where d and n_g indicate the polynomial chaos degree and the number of germs.

KLE truncation error	0.1		0.01		0.001	
No. of terms	KLE	PCE (Hermite)	KLE	PCE (Hermite)	KLE	PCE (Hermite)
Gauge	130	330 ($n_g = 4$,$d = 7$)	314	1001 ($n_g = 4$,$d = 10$)	722	2002 ($n_g = 5$, $d = 9$)
Superelevation	34	120 ($n_g = 3$,$d = 7$)	173	495 ($n_g = 4$,$d = 8$)	325	1287 ($n_g = 5$, $d = 8$)
Horizontal curvature	72	210 ($n_g = 4$,$d = 6$)	129	495 ($n_g = 4$,$d = 8$)	217	715 ($n_g = 4$, $d = 9$)
Vertical curvature	50	165 ($n_g = 3$,$d = 8$)	100	330 ($n_g = 4$,$d = 7$)	160	495 ($n_g = 4$,$d = 8$)

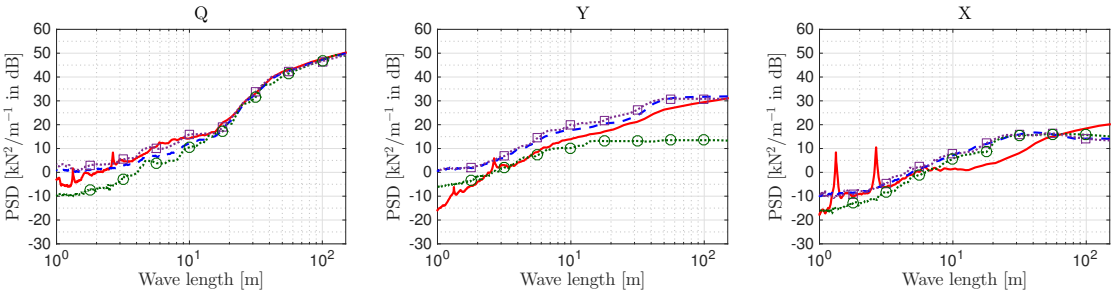

Figure 26. PSD of contact forces, front wheelset in alignment, constant velocity. Experimental data (red line), numerical simulations with track geometry irregularities with KLE error equal to 10% (dotted green line with circle markers), 1% (dashed blue line) and 0.1% (dotted violet line with square markers).

3.4. *Simulation with wheel irregularities*

The presence of wheel irregularities can lead to significant contact forces variations. A large wheel flat defect implies large variations on the vertical forces (and their spectrum) because of the impact force induced by a brutal change of the wheel shape [42].

When the wheel untrueness is an inconstant nominal wheel radius (that varies with the wheel rotation angle), periodic changes of the contact forces are produced [43]. This is the situation observed on the experimental spectral densities. Even a small variation on the radius (0.1 mm for instance) induces a variation of the longitudinal creepage (which is normally very small in a straight track at constant running velocity) and so the longitudinal forces. The vertical equilibrium is affected by a very small wheelset roll angle caused by a different rolling radius of the two wheels (approximatively 0.004° for a 0.1 mm radius difference) that lightly affects the track vertical forces.

Since the wheel nominal diameters of the motor coach (not used for the simulations in this work) are slightly larger (0.46 m) than the passenger car, the peaks appear at shifted wavelengths (Figure 27).

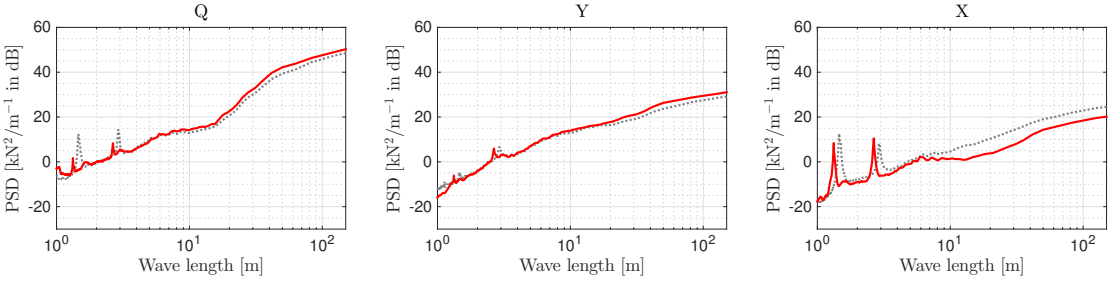

Figure 27. Experimental PSD of the leading wheelsets of the passenger car (red line) and motor coach (dotted grey line).

Numerical simulations with wheel arbitrary untrueness (nominal radius variable as in Figure 28) on the front wheelset of the leading car are performed and compared with the measurements (Figure 29). The location in frequency of the peaks is well reproduced. Note that the identification of irregularities of the wheels is out of the scope of this paper, so no effort has been devoted to fine tune the amplitude of the peaks.

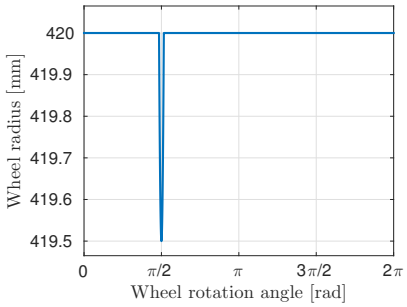

Figure 28. Wheel untrue used for the numerical simulations.

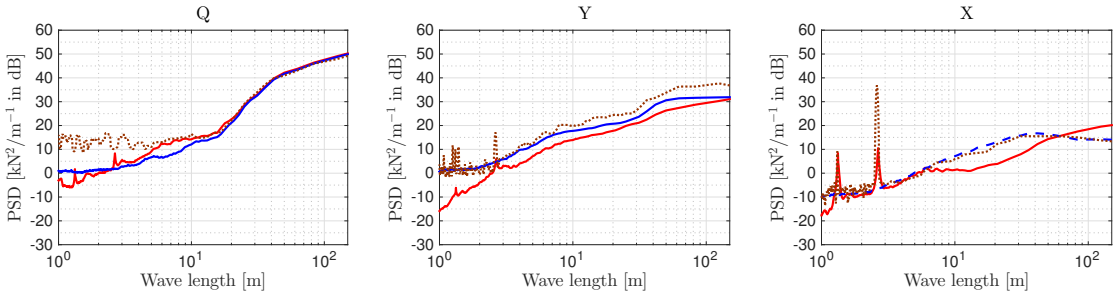

Figure 29. PSD of contact forces, front wheelset in alignment, constant velocity. Experimental data (red line), numerical simulations with track geometry irregularities without (dashed blue line) and with (dotted brown line) wheel untrueness.

4. Conclusion

The steps to lead to a stochastic characterisation of the track geometry irregularities of a railway network have been presented in this work. A large set of experimental measurements is used to model the irregularities as random fields. The model is able to capture the statistical and the spatial variability of the irregularities on the considered track.

Another set of measurements is used to validate the stochastic model of the geometry. The contact forces are measured by another recording train on the same railway network. The stochastic irregularities can be used as inputs of a railway dynamics software to compute the wheel-rail contact forces. The numerical PSDs are very close to the experimental ones when the irregularities are considered in the simulations. The improvement, when comparing the simulations with a theoretical track, is above one order of magnitude and is obtained by considering all the other parameters (such as rail and wheel profiles, friction coefficient and vehicle suspensions stiffness) as deterministic. This means that the track geometry irregularities are the most influential variable parameter.

A further work will consist in investigate on the influence of the track irregularities on the rail rolling contact fatigue, which strongly depends on the wheel-rail contact stresses. As shown in this paper, a deterministic model is not able to capture the real variability of the contact forces (and so the rail surface stresses). The stochastic irregularities model will allow to improve the rail fatigue life predictions.

The method described in the paper only considers the geometry irregularities (i.e. the position of the rails) as stochastic fields modelled from measurements. As shown, when the geometry irregularities are taken into account, a strong improvement of the spectral densities of the contact forces is observed. Other kinds of track irregularities (such as rail corrugation, rail cant variations and joints) could be introduced into the model to further

improve the comparison. If these quantities are correlated to the geometry irregularities, then they will be modelled as cross-correlated random fields.

References

[1] Lei X, Noda NA. Analyses of dynamic response of vehicle and track coupling system with random irregularity of track vertical profile. Journal of Sound and Vibration. 2002;258(1):147–165.

[2] Gullers P, Andersson L, Lundén R. High-frequency vertical wheel-rail contact forces-Field measurements and influence of track irregularities. Wear. 2008;265(9-10):1472–1478.

[3] Zhai W, Wang K, Cai C. Fundamentals of vehicle-track coupled dynamics. Vehicle System Dynamics. 2009;47(11):1349–1376.

[4] Perrin G, Soize C, Duhamel D, Funfschilling C. Quantification of the influence of the track geometry variability on the train dynamics. Mechanical Systems and Signal Processing. 2015;60:945–957.

[5] Yang X, Gu S, Zhou S, Yang J, Zhou Y, Lian S. Effect of track irregularity on the dynamic response of a slab track under a high-speed train based on the composite track element method. Applied Acoustics. 2015;99:72–84.

[6] Evans JR, Burstow MC. Vehicle / track interaction and rolling contact fatigue in rails in the UK. Vehicle System Dynamics. 2006;44:708–717.

[7] Li Z, Zhao X, Esveld C, Dollevoet R, Molodova M. An investigation into the causes of squats Correlation analysis and numerical modeling. Wear. 2008;265:1349–1355.

[8] Karttunen K, Kabo E, Ekberg A. The influence of track geometry irregularities on rolling contact fatigue. Wear. 2013;314(1-2):78–86.

[9] Jin XS, Wen ZF, Wang KY. Effect of track irregularities on initiation and evolution of rail corrugation. Journal of Sound and Vibration. 2005;285(1-2):121–148.

[10] Sun YQ, Roach D. Effect of track geometry irregularities on wheel-rail impact forces. In: Conference on Railway Engineering. Darwin; 2004.

[11] Grassie S. Measurement of railhead longitudinal profiles: a comparison of different techniques. Wear. 1996;191:245–251.

[12] Fröhling RD. Measurement, interpretation and classification of South African track geometry. Vehicle System Dynamics. 1995;24(Supplement 1):133–145.

[13] Haigermoser A, Luber B, Rauh J, Gräfe G. Road and track irregularities: measurement, assessment and simulation. Vehicle System Dynamics. 2015;53(7):878–957.

[14] Nielsen J, Berggren E, Lölgen T, Müller R, Stallaert B, Pesqueux L. Overview of Methods for Measurement of Track Irregularities Important for Ground-Borne Vibration. Railway Induced Vibration Abatement Solutions; 2013. Report No.: SCP0-GA-2010-265754.

[15] Claus H, Schiehlen W. Modeling and Simulation of Railway Bogie Structural Vibrations. Vehicle System Dynamics. 1998;29(sup1):538–552.

[16] Iyengar BRN, Jaiswap OR. Random field modeling of track irregularities. Journal of Tranport ation Engineering. 1995;121:303–308.

[17] Zhu M, Cheng X, Miao L, Sun X, Wang S. Advanced Stochastic Modeling of Railway Track Irregularities. Advances in Mechanical Engineering. 2013;.

[18] Majka M, Hartnett M. Dynamic response of bridges to moving trains: A study on effects of random track irregularities and bridge skewness. Computers and Structures. 2009;87(19-20):1233–1252.

[19] Shinozuka M, Deodatis G. Simulation of stochastic processes by spectral representation. Applied Mechanics Reviews. 1991;44(4):191–204.

[20] Perrin G, Soize C, Duhamel D, Funfschilling C. Track irregularities stochastic modeling. Probabilistic Engineering Mechanics. 2013;34:123–130.

[21] Loève M. Probability theory. 4th ed. Springer-Verlag; 1977.

[22] Ghanem RG, Spanos PD. Stochastic Finite Elements: A Spectral Approach. New York, NY: Springer New York; 1991.

[23] Pombo J, Ambrósio J. An alternative method to include track irregularities in railway vehicle dynamic analyses. Nonlinear Dynamics. 2012;68(1-2):161–176.

[24] Luber B, Haigermoser A, Grabner G. Track geometry evaluation method based on vehicle response prediction. Vehicle System Dynamics. 2010;48(sup1):157–173.

[25] Li MXD, Berggren EG, Berg M, Persson I. Assessing track geometry quality based on wavelength spectra and track-vehicle dynamic interaction. Vehicle System Dynamics. 2008;46(sup1):261–276.

[26] Kanehara H, Fujioka T. Measuring rail/wheel contact points of running railway vehicles. Wear. 2002;

253(1-2):275–283.

[27] Aknin P, Chollet H. A new approach for the modelling of track geometry recording vehicles and the deconvolution of versine measurements. In: The International Association for Vehicle System Dynamics (IAVSD). Pretoria; 1999.

[28] Mauer L. Determination of Track Irregularities and Stiffness Parameters with Inverse Transfer Functions of Track Recording Vehicles. Vehicle System Dynamics. 1995;24:117–132.

[29] Panunzio AM, Puel G, Cottereau R, Quost X. A stochastic model of the railway track geometry. In: The International Association for Vehicle System Dynamics (IAVSD). Graz, Austria: Taylor & Francis; 2015.

[30] Liu X, Tap K, Tian X, Li H. Characteristic Analysis of the PSD of Track Irregularity on Ballastless Track in High-speed Railway. In: International Conference on Railway Engineering. Beijing; 2012.

[31] Weston P, Ling C, Roberts C, Goodman C, Li P, Goodall R. Monitoring vertical track irregularity from in-service railway vehicles. Proceedings of the Institution of Mechanical Engineers, Part F: Journal of Rail and Rapid Transit. 2007;221(1):75–88.

[32] Weston P, Ling C, Goodman C, Roberts C, Li P, Goodall R. Monitoring lateral track irregularity from in-service railway vehicles. Proceedings of the Institution of Mechanical Engineers, Part F: Journal of Rail and Rapid Transit. 2007;221(1):89–100.

[33] Zhang ZC, Lin JH, Zhang YH, Zhao Y, Howson WP, Williams FW. Non-stationary random vibration analysis for train-bridge systems subjected to horizontal earthquakes. Engineering Structures. 2010; 32(11):3571–3582.

[34] Lin J, Chen J, Su Y. Theory analysis and test research of Chinese main track irregularities PSD. Chinese Journal of Mechanical Engineering. 2004;40(1):174–178.

[35] Soize C. Identification of high-dimension polynomial chaos expansions with random coefficients for non-Gaussian tensor-valued random fields using partial and limited experimental data. Computer Methods in Applied Mechanics and Engineering. 2010;199(33-36):2150–2164.

[36] Perrin G, Soize C, Duhamel D, Funfschilling C. Identification of polynomial chaos representations in high dimension from a set of realizations. SIAM Journal on Scientific Computing. 2012;34:2917–2945.

[37] Kullback S, Leibler R. On information and sufficiency. The Annals of Mathematical Statistics. 1951; 22(1):79–86.

[38] Cho H, Venturi D, Karniadakis GE. Karhunen-Loève expansion for multi-correlated stochastic processes. Probabilistic Engineering Mechanics. 2013;34:157–167.

[39] Ayasse J, Chollet H. Determination of the wheel rail contact patch in semi-Hertzian conditions. Vehicle System Dynamics. 2005;43(3):161–172.

[40] Simon S. De la dynamique ferroviaire à l'accommodation microstructurale du rail Phd thesis. Institut national des sciences appliquées de Lyon; 2014 (in French).

[41] Panunzio AM, Puel G, Cottereau R, Simon S, Quost X. Wheel-Rail Contact Parameters Sensitivity Analysis with Stochastic Track Geometry. In: Civil-Comp Press Conference on Railway Technology: Research, Development and Maintenance. Cagliari, Italy; 2016.

[42] Uzzal RUA, Ahmed W, Rakheja S. Dynamic Analysis of Railway Vehicle-Track Interactions due to Wheel Flat with a Pitch-Plane Vehicle Model. Journal of Mechanical Engineering. 2008;39(2):86–94.

[43] Newton SG, Clark RA. An investigation into the dynamics effects on the track of the wheelflats on railway vehicles. Journal of Mechanical Engineering Science. 1979;21:287–297.

[44] Makhoul J. On the eigenvectors of symmetric Toeplitz matrices. IEEE Transactions on Acoustics, Speech, and Signal Processing. 1981;29(4):868–872.

[45] Unser M. On the approximation of the discrete Karhunen-Loeve transform for stationary processes. Signal Processing. 1984;7:231–249.

Appendix A: Measurement train V355

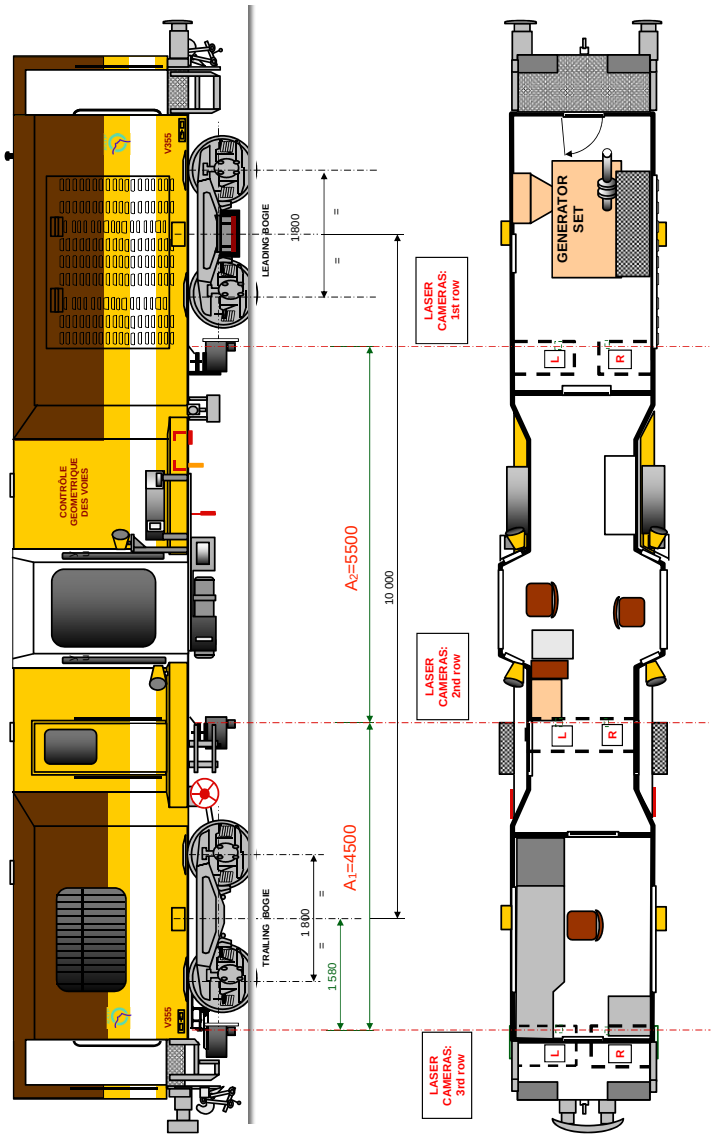

Figure 30. Measurement train, all the lengths are expressed in millimetres.

Appendix B: Continuity of the generated fields

Let l_l and l_r be respectively the left and the right random limits of the generated field $g(s)$ in Equation 19 at the breaking point kl (with k going from 1 to $n-1$):

$$\begin{aligned} l_l &= \lim_{s \to kL^-} g(s) = \boldsymbol{\Phi}(L)\sqrt{\boldsymbol{\Lambda}}\tilde{\boldsymbol{H}}^{(k)} \\ l_r &= \lim_{s \to kL^+} g(s) = \boldsymbol{\Phi}(0)\sqrt{\boldsymbol{\Lambda}}\tilde{\boldsymbol{H}}^{(k+1)} \end{aligned} \tag{21}$$

By using the expectations in Equation 20 and the definition of the KLE in Equation 5, it follows that, when the number of KLE terms is enough large to give a small truncation error:

$$\begin{aligned} &\mathbb{E}[l_l] = \mathbb{E}[l_r] = 0 \\ &\mathbb{E}[l_l^2] = \boldsymbol{\Phi}(L)\sqrt{\boldsymbol{\Lambda}}\,\mathbb{E}[\tilde{\boldsymbol{H}}^{(k)}(\tilde{\boldsymbol{H}}^{(k)})^{\mathrm{T}}]\sqrt{\boldsymbol{\Lambda}}\,\boldsymbol{\Phi}(L)^{\mathrm{T}} = \boldsymbol{\Phi}(L)\boldsymbol{\Lambda}\,\boldsymbol{\Phi}(L)^{\mathrm{T}} \approx C(L,L) \\ &\mathbb{E}[l_r^2] = \boldsymbol{\Phi}(0)\sqrt{\boldsymbol{\Lambda}}\,\mathbb{E}[\tilde{\boldsymbol{H}}^{(k+1)}(\tilde{\boldsymbol{H}}^{(k+1)})^{\mathrm{T}}]\sqrt{\boldsymbol{\Lambda}}\,\boldsymbol{\Phi}(0)^{\mathrm{T}} = \boldsymbol{\Phi}(0)\boldsymbol{\Lambda}\,\boldsymbol{\Phi}(0)^{\mathrm{T}} \approx C(0,0) \end{aligned} \tag{22}$$

As shown in [44, 45], the stationarity implies that the KLE modes are alternatively symmetric or anti-symmetric ($\varphi_i(s) = \pm\varphi_i(L-s)$). Because of this property, it follows that:

$$\boldsymbol{\Phi}(L)\boldsymbol{\Lambda}\,\boldsymbol{\Phi}(L)^{\mathrm{T}} = \boldsymbol{\Phi}(0)\boldsymbol{\Lambda}\,\boldsymbol{\Phi}(0)^{\mathrm{T}} \Longrightarrow \mathbb{E}[l_l^2] = \mathbb{E}[l_r^2] \approx C(|L-L|) = C(|0-0|) = C(0) \tag{23}$$

By using the definition of the matrix $\mathbf{K}$ (Equation 16) and the expectations in Equation 20, it follows that:

$$\begin{aligned} \mathbb{E}[l_l l_r] &= \boldsymbol{\Phi}(L)\sqrt{\boldsymbol{\Lambda}}\,\mathbb{E}[\tilde{\boldsymbol{H}}^{(k)}(\tilde{\boldsymbol{H}}^{(k+1)})^{\mathrm{T}}]\sqrt{\boldsymbol{\Lambda}}\,\boldsymbol{\Phi}(0)^{\mathrm{T}} \\ &= \boldsymbol{\Phi}(L)\sqrt{\boldsymbol{\Lambda}}\mathbf{K}\sqrt{\boldsymbol{\Lambda}}\,\boldsymbol{\Phi}(0)^{\mathrm{T}} \approx \tilde{C}(|L-0-L|) = C(0) \end{aligned} \tag{24}$$

From Equations 23 and 24, it follows that the left and right limits are approximate equal:

$$\mathbb{E}[l_l^2] = \mathbb{E}[l_r^2] \approx \mathbb{E}[l_l l_r] \Longleftrightarrow l_l \approx l_r \tag{25}$$

When $M \to \infty$, the approximate equalities in the Equations 22-25 become exact equalities. Each generated realisation of the random field is thus continuous when $M \to \infty$:

$$\lim_{M \to \infty} (l_l - l_r) = 0 \tag{26}$$

Note that the KLE yields the best such basis in the sense that it minimizes the total mean squared error (Equation 12). The basis is optimal for the decomposition of the covariance function $C(|s-t|)$. The Equation 16 is a decomposition of $\tilde{C}(|s-t-L|)$ into a basis which is optimal for $C(|s-t|)$. For this reason:

$$\boldsymbol{\Phi}(L)\sqrt{\boldsymbol{\Lambda}}\mathbf{K}\sqrt{\boldsymbol{\Lambda}}\,\boldsymbol{\Phi}(0)^{\mathrm{T}} \leq \boldsymbol{\Phi}(L)\boldsymbol{\Lambda}\,\boldsymbol{\Phi}(L)^{\mathrm{T}} = \boldsymbol{\Phi}(0)\boldsymbol{\Lambda}\,\boldsymbol{\Phi}(0)^{\mathrm{T}} \tag{27}$$

This fact also comes from the Cauchy-Schwarz inequality: $\mathbb{E}[l_l l_r]^2 \leq \mathbb{E}[l_l^2]\,\mathbb{E}[l_r^2]$.

In numerical applications, when a large number of KLE terms is chosen, the error made by considering the previous approximate equalities as exact equalities is small. In this work this error is evaluated through the following quantity (r) for the four generated fields:

$$r = 1 - \frac{\boldsymbol{\Phi}(L)\sqrt{\boldsymbol{\Lambda}}\mathbf{K}\sqrt{\boldsymbol{\Lambda}}\,\boldsymbol{\Phi}(0)^{\mathrm{T}}}{\boldsymbol{\Phi}(L)\boldsymbol{\Lambda}\,\boldsymbol{\Phi}(L)^{\mathrm{T}}} \tag{28}$$

In Figure 31, the value of this quantity, calculated for different numbers of KLE terms and for each field, is shown. For the numbers of KLE terms chosen for the generation (Table 1), the order of magnitude of r is 10^{-2}.

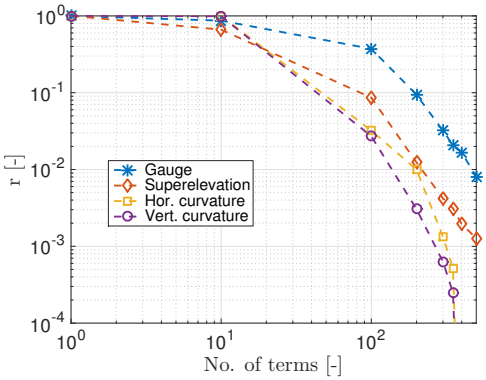

Figure 31. Evaluation of the quantity r, defined in Equation 28, for different numbers of Karhunen-Loève terms and for each generated field.